![Aalto University logo]

Markou, Athanasios A.; Baroudi, Djebar; Cheng, Qiang; Bordbar, Hadi

Unfolding the dynamics of free-falling folded chain : Experiments and simulations

Unfolding the dynamics of free-falling folded chain: Experiments and simulations

Athanasios A. Markou [a],[*], Djebar Baroudi [a], Qiang Cheng [b], Hadi Bordbar [a]

[a] *Department of Civil Engineering, Aalto University, Espoo, Finland*
[b] *Department of Mechanical Engineering, Aalto University, Espoo, Finland*

ABSTRACT

Contrary to educated intuition, the tip of a free-falling U-folded chain accelerates faster than gravity without violating the Newtonian laws. In the current work, we study the dynamics of a free-falling U-folded chain experimentally as well as numerically. To this end, high-speed imaging (up to 10 000 fps) is used to capture the chain's falling tip by using different openings between the two tips of the chain. Thanks to high-speed digital imaging, the detailed geometry of the dynamic unfolding is captured. The post-processing of captured images has provided detailed quantitative temporal data for displacement, velocity, and acceleration of the falling tip of the chain. The experimental observations have revealed the various phases of dynamics of the falling U-folded chain, including unfolding, whipping, and rebounding phases for the first time. Furthermore, a Henky-type model is developed to capture the associated phenomena related to these phases, such as rebound effect, whip effect, local buckling, and transverse wave propagation. The model that includes nonlinear elastic, dissipative and bilateral gap-contact features, could successfully capture the experimentally observed phases and phenomena of the unfolding dynamics qualitatively.

1. Introduction

The dynamics of the variable-mass systems involve applications in a wide variety of fields, such as rocket theory [1], astronomy [2], biology [3], physics [4], engineering [5], and economics [6], to mention but a few. The complexity of the treatment of such systems has generated many challenges and misunderstandings among the research community [7]. In the case of a folded chain, its initial U-shape is created when the chain is suspended by its two ends at the same level, see Fig. 1. As one of its ends is released, a variable part of the U-folded chain is in motion, behaving like a variable-mass system [8]. Due to momentum balance, the falling chain tip accelerates faster than the gravitational acceleration g as the moving part becomes smaller over time [9]. Due to this counter-intuitive fact, falling chains have attracted the research community's attention in recent years, [10,11]. To this end, several experimental and numerical efforts have been reported in the literature. Calkin and March used different types of chains to measure the tension at the fixed end of a free-falling U-folded chain, [9]. The authors observed that the maximum tension in the chain was 25 times the weight of the chain itself. Additionally, they observed that the falling time of the 1.993 m long folded chain was 84.7% of the free-falling time. In this way, they pointed out that the falling chain problem had been solved incorrectly almost 160 years ago [12].

Kagan and Kott employed strobe photography to study the acceleration of a bungee jumper by using three ropes with different

thicknesses and a chain, [13]. The different types of ropes were meant to investigate the effect of stiffness, while the chain was used for its minimal stiffness. Their theoretical model agreed fairly well with the experiments and predicted that for a bungee mass to jumper mass ratio equal to 5, the acceleration would be equal to 6.6 g.

Similarly, Schargel et al. [14] tested a 2.41 m long chain with a ball attached at its falling tip in parallel with a free-falling steel ring in a dark room by using stroboscopic flash light of 20 Hz. The authors observed that the endpoint of the chain reaches a maximum velocity of 17 m/s $\approx$ 60 km/h, which is 2.4 times faster than the free falling maximum velocity, which was around 7 m/s $\approx$ 25 km/h. They also developed a planar lumped model of a folded chain comprising approximately rectangular rings to capture the tip's position. Rotational viscous dampers were used to match the experimental results, but there was no contact model to simulate the contact between the links.

Taft investigated the propagation of waves through a cracking whip, [15]. To understand why the whip cracks, he decided to test a similar phenomenon: the falling chain. In the case of the chain, the observed tip acceleration was higher than g, while in the case of the whip, the cracking sound was produced by the supersonic velocity of its tip [16]. Both phenomena were explained by the dynamics of the variable-mass systems.

In a similar manner, Tomaszewski and Pieranski used a 1 m long chain to study the dynamics of the falling chain, [17]. The difference
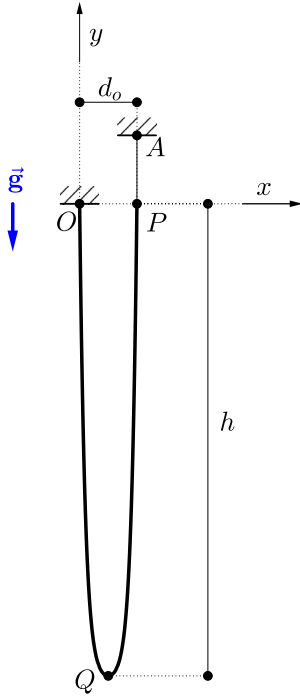

Fig. 1. U-folded chain, where OQP is the chain, AP is a very thin string, and $OP = d_o$ is the opening.

in this experimental work compared to the previous ones was that the initial position of the free falling chain tip was at a higher level than the fixed end of the chain. After qualitative calibration of their numerical model with the experimental data, they observed a peak in the velocity when the chain became almost straight. They developed a discrete two-dimensional model to capture the behavior of the falling chain. The model included rigid links without elasticity and dissipation. On the other hand, Fritzkowski and Kamiński [18] developed a model comprising rigid parts and linear elastic springs connected at frictionless joints to study the dynamics of ropes. The model did not account for the bending rigidity of the joints. A year later, Tomaszewski et al. [19] repeated the experiments with the same chain, but this time the two ends of the U-folded chain were at the same level. Furthermore, they used four different initial configurations by varying the horizontal opening d_o between the two ends (see Fig. 1) of the U-folded chain, with the largest value being $0.999L$. For this largest d_o, by analyzing the recorded video with 50 frames per second (fps) they reported that the motion of the chain is identical to the free-falling body as the system is not a variable-mass one anymore.

Géminand and Vanel [20] modified the same chain experimental setup as that of Calkin and March [9] to measure the horizontal and vertical components of the force applied to the fixed end of the chain. They concluded that the maximum force in horizontal and vertical components does not occur at the same time instant when d_o (see Fig. 1) is large. This time lag was explained by the fact that the chain behaves more like a pendulum and the maximum tension occurs when the chain is not vertical.

Using moderate-speed imaging of 30 fps, Heck et al. [21] investigated the physics of the bungee jumping and pointed out that when the mass of the bungee is taken into account the jumper's acceleration is greater than g. They used accelerometers to investigate the fall of a wooden block attached to a chain. The results clearly showed that the acceleration of the block was greater than g. The block reached its maximum acceleration when the chain was almost stretched with a value of 24 m/s^2. Additionally, they compared the free fall of a wooden block with a wooden block attached to a chain by using high-speed

imaging with rate 300 fps. The results showed that the chained block falls faster than the free falling one.

De Sousa et al. [22] used three different types of chains to investigate the free falling of the U-folded chain and a chain hanging off from the edge of a table. The authors observed that the maximum value of the tension in the U-folded chain was achieved at the end of the fall and it was larger than 50 times the weight of the chain. Using 1000 fps, Yokohama [23] linked the behavior of the free falling of the U-folded chain with the chain fountain pointing out that both phenomena are consequence of the energy conserving dynamics of linear chains. The author also reported that the tip of the chain is falling faster than the time required for its free fall. Domnyshev et al. [24] used two different types of chains with different diameter to investigate the free falling of the U-folded chain. High-speed imaging was used to record the experiment with rate 500 fps.

Guttner and Pesce [25] used the principle of virtual work with D'Alembert's principle to extend Hamilton's principle and Lagrange's equations for discrete variable-mass systems. Lee et al. [26] extended the classical formulation of the falling chain to account for the additional kinetic energy introduced from the jump of each chain link. The authors validated the derived formulation against experimental observations to evaluate the total falling time of the tip and the maximum tension at the fixed end of the chain. Along the same lines, Virga [27] studied the dissipative dynamics in 1D inextensible continuum string medium for chain paradoxical cases, including the falling chain. The author extended the Rayleigh's dissipation principle to account for singularities in the velocity field.

As it is widely reported in the literature, all experiments have measured an acceleration larger than g for the free-falling U-folded chain. Additionally, the discrepancies between the various force measurements on the fixed end of the chain are essentially due to different dissipation mechanisms that occur in the fixing system. Nevertheless, the maximum video recording speed for the free falling of the folded chain reported in the literature was 1000 fps. In the present study, we use a high-speed camera with a recording speed up to 10 000 fps, which is ten times faster than what has ever been reported in the literature. For the first time, the various dynamical patterns of the free-falling chain are captured and addressed along with the associated physical phenomena.

Furthermore, most of the models reported in the literature do not simultaneously account for axial and rotational stiffness and dissipation in addition to contact between the links. Alternatively, models developed for granular material [28] could be used, if they account for nonlinear elasticity, dissipation and bilateral gap-contact features. Hence, a Henky-type model [29] with all the aforementioned features is developed to capture the qualitative behavior of the experimental results. In the next section, the experimental setup is presented along with the experimental results, followed by the numerical model, the results, and the conclusions.

2. Experiments

The experiments of the free-falling folded chain took place in the laboratory of the Engineering School at Aalto University, Espoo, Finland. The experimental set-up is shown in Fig. 2. The chain used in the experiments, was a metallic ball chain, see Fig. 3. As shown in Fig. 1, one end of the chain, point O, is mounted rigidly, while the other one, i.e. point P in Fig. 1, is connected with a very thin string AP to a rigid support (point A). In order to initiate the falling of the folded chain, the string was burnt, and the tip of the chain, i.e. point P, was released with zero initial velocity.

The dynamics of the folded chain are captured by a high-speed color camera (Photron Fastcam SA-Z [30]) equipped with a Nikon lens (Nikon AF Nikkor 180 mm f/2.8), which has the ability to capture high-resolution digital images at ultra-high speed. The camera has a 1-megapixel CMOS image sensor with a full resolution of 1024×1024

Fig. 2. The experimental set-up with the high speed camera (Photron SA-Z) and the folded chain in its initial configuration.

Table 1
The series of tests of the free-falling folded chain with their initial opening d_o (see Fig. 1) and fps.

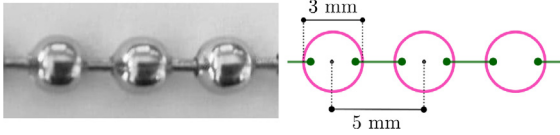| Test	d_o (m)	fps
T1	0.045	10000
T2	0.045	2000
T3	0.045	2000
T4	0.087	2000
T5	0.128	2000
T6	0.045	2000

Fig. 3. The ball chain (left) used in the experiments and a sketch (right) of the connections between the balls of the chain.

pixels at 2000 fps. In this study, 2000 fps with an exposure time of 0.5 ms is selected to balance the chain moment and time scale. For the 10 000 fps case, we also use a full resolution of 1024 × 1024 pixels with an exposure time of 0.1 ms. More specifically, the record duration is 5 s, which means 10 000 frames for the case of 2000 fps. The scale factor between millimeter and pixel is around 1.58 mm/pixel. A black curtain was used to create a black background to avoid the random noise from the environment. Two powerful halogen lights are used as the light source to provide homogeneous light along the length of the chain.

The experimental session consists of 6 tests, namely T1, T2, T3, T4, T5, and T6 with different initial openings, i.e. d_o in Fig. 1, and fps as listed in Table 1. The tests T1, T2, T3, and T6 with initial openings $d_o = 0.045$ m were repeated three times, while the tests T4 and T5 were implemented once, with initial opening $d_o = 0.087$ m and 0.128 m, respectively. In the following, only tests T2, T3, and T5 will be considered due to their distinct opening d_o.

3. Numerical model

A non-linear discrete mechanical model is developed to simulate the dynamic behavior of the free-falling folded chain. The model consists of N spherical masses linked by short rods, see Fig. 4. The discrete mass system is lumped to nodal masses m_i with coordinates (x_i, y_i), which are the independent variables of the resulting discrete dynamical problem with $i = 1$ to $2N$. The coordinates, displacements, velocities
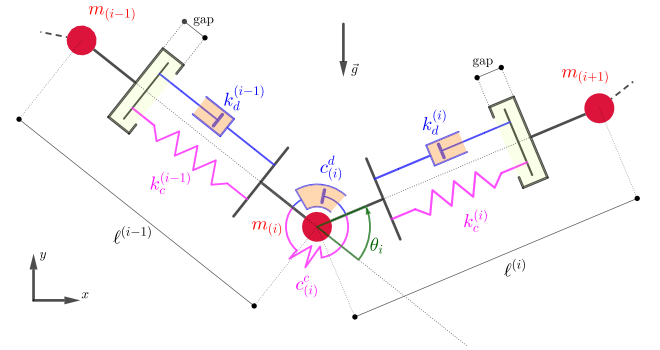

Fig. 4. A sketch showing the concept of the developed lumped model for the dynamics of the free-falling folded chain.

and accelerations of the lumped masses are denoted by $x(t)$, $u(t)$, $\dot{u}(t) = \dot{x}$ and $\ddot{u}(t) = \ddot{x}$, respectively. The model is two-dimensional; therefore the vectors will have a length equal to $2N$. The mechanical interaction between linked lumped masses is modeled with rheological models, comprising axial and rotational non-linear springs, for the conservative forces, along with non-linear translational and rotational dashpots, for the dissipative forces Fig. 4. More specifically, the model accounts for: smooth axial stiffening, bilateral gap-contact (between the beads), smooth interpenetration stiffening (collision of beads), smooth rotational stiffening ("locking" of chain) and dissipation (axial and rotational) that can vary: from Coulomb friction ($n = 0$) to viscosity ($n = 1$) through nonlinear viscosity ($0 < n < 1$), see Sections 3.1.1, 3.1.3. By using the principle of virtual work in conjunction with d'Alembert's principle

$$\delta W_{\text{int}} + \delta W_{\text{ext}} = \delta W_{\text{acc}}, \forall \delta \mathbf{u} \tag{1}$$

the equations of motion of the system are derived

$$\boldsymbol{M}\ddot{\boldsymbol{u}} = \boldsymbol{f}(\boldsymbol{u}, \dot{\boldsymbol{u}}, t) \tag{2}$$

where $\boldsymbol{M}$ is the global diagonal mass matrix of size $2N \times 2N$, comprising contributions from the local nodal mass matrices, e.g. for the node i is given by $\mathbf{M}_i = \text{diag}(m_i, m_i)$.

The global generalized nodal force vector comprises contributions of internal ($\boldsymbol{f}_{int}$) and external forces ($\boldsymbol{f}_{ext}$), that both have conservative ($\boldsymbol{f}^{(c)}$) and dissipative ($\boldsymbol{f}^{(d)}$) parts:

$$\boldsymbol{f}(\boldsymbol{u}, \dot{\boldsymbol{u}}, t) = \boldsymbol{f}_{int} + \boldsymbol{f}_{ext}; \quad \boldsymbol{f}(\boldsymbol{u}, \dot{\boldsymbol{u}}, t) = \boldsymbol{f}^{(c)} + \boldsymbol{f}^{(d)} \tag{3}$$

The global force vector $\boldsymbol{f}(\boldsymbol{u}, \dot{\boldsymbol{u}}, t)$ is assembled from elementary contributions of the internal nodal forces, which resist to axial stretching, and

bending, while their are denoted as:

$$f_{int} = f_{int}(N) + f_{int}(M) \tag{4}$$

where N denotes axial force and M bending moment. The external forces are due to gravity f_g and to any other imposed forces f_e, such as air drag for instance and they are given as:

$$f_{ext}(u, \dot{u}, t) = f_g + f_e \tag{5}$$

The equation of motion, Eq. (2), is strongly nonlinear time-dependent due to nonlinear constitutive laws and non-smooth with gap-contact model, which is approximated model using smooth indicator functions. The order of the equation of motion is reduced to one prior time-integration by taking nodal velocities $\mathbf{v}$ as auxiliary variables

$$\mathbf{v} = \dot{\mathbf{u}} \tag{6}$$

This is practical because the mass-matrix is diagonal and invertible, $\mathbf{M}^{-1} = \operatorname{diag}(1/M_{ii})$, and not expensive to compute. The resulting first order non-linear differential equation (ODE):

$$\dot{\mathbf{y}} \equiv \begin{bmatrix} \dot{\mathbf{v}} \\ \dot{\mathbf{u}} \end{bmatrix} = \begin{bmatrix} \mathbf{M}^{-1}\mathbf{f}(\mathbf{u}, \mathbf{v}, t) \\ \mathbf{v} \end{bmatrix} \equiv f(\mathbf{y}, \dot{\mathbf{y}}, t); \quad \mathbf{y} = [\mathbf{v}, \mathbf{u}]^{\mathrm{T}} \tag{7}$$

is implicitly time-integrated using Matlab [31] routine `ode15s` [32, 33], which is a variable-step, variable order (VSVO) solver using numerical differentiation formulas of order 1 to 5. This routine solves efficiently stiff and non-stiff differential equations with and without algebraic constraints (DAE).

3.1. Internal force vectors

The global nodal force vector is assembled from elementary contributions from the nodal-wise force resultants. In the following, the superscripts and the subscripts will refer to elements and nodes, respectively. The internal nodal force $f(N)$ results from length change $\Delta \ell^i$ and is formed in an element-wise manner. Each element links two consecutive nodes x_i and x_{i+1} with length $\ell^i = \|x_{i+1} - x_i\|$. The elongation of an element $\Delta \ell^i$ is determined once its nodal displacements u^i are defined:

$$\Delta \ell^i = \mathbf{R}^i \cdot \mathbf{u}^i \equiv q^i \tag{8}$$

where $[\mathbf{R}^i] = [\sin \theta_i, -\cos \theta_i, \sin \theta_i, \cos \theta_i]$, $\sin \theta_i = (x_{i+1} - x_i)/\ell^i$, $\cos \theta_i = (y_{i+1} - y_i)/\ell^i$ is a projection matrix to project element nodal displacements along the element length $\vec{\ell}^i$ containing director cosines of the element and θ_i is the node-wise relative rotation between two consecutive elements, see Fig. 4.

On the contrary, the internal nodal force vector resulting from bending, $f(M)$, is formed node-wise depending on the rotation θ_i. Such rotation θ_i is defined by the inverse function of:

$$\cos \theta_i = \frac{\vec{\ell}^i \cdot \vec{\ell}^{i-1}}{\ell^i \cdot \ell^{i-1}}, \quad \vec{\ell}^j = (x_{j+1} - x_j) \tag{9}$$

The elementary force vectors are derived directly by applying the virtual work principle.

3.1.1. Axial internal nodal force

The axial internal nodal forces $f^i(N)$ comprise column vectors of size (4×1) given by

$$\delta W_{\mathrm{int}}^{(N)} = \sum_i N^i \delta(\Delta \ell^i) = \sum_i N^i \delta(\mathbf{R}^i \mathbf{u}^i) = \sum_i \underbrace{N^i (\mathbf{R}^i + \mathbf{u}^{(i)\mathrm{T}}[\nabla_{x^i} \mathbf{R}^i])}_{\equiv f^{(i)\mathrm{T}}(N)} \cdot \delta \mathbf{u}_i \tag{10}$$

$$f^i(N) = (\mathbf{R}^{(i)\mathrm{T}} + [\nabla_{x^i} \mathbf{R}^i]^{\mathrm{T}} \mathbf{u}_i) \cdot [N_c^i + N_d^i] \tag{11}$$

where $[\nabla_{x^i}]$ is the gradient vector with respect to nodal coordinates $x^i = (x_i, x_{i+1})$. The scalar terms N_c^i and N_d^i represent the internal axial forces (conservative and dissipative) in the element, which are defined by adequate constitutive laws:

$$N_d^i = k_d^i \cdot \left| \dot{q}^i / \dot{q}_{\mathrm{ref}} \right|^n \cdot \operatorname{sign}(\dot{q}^i) \tag{12}$$
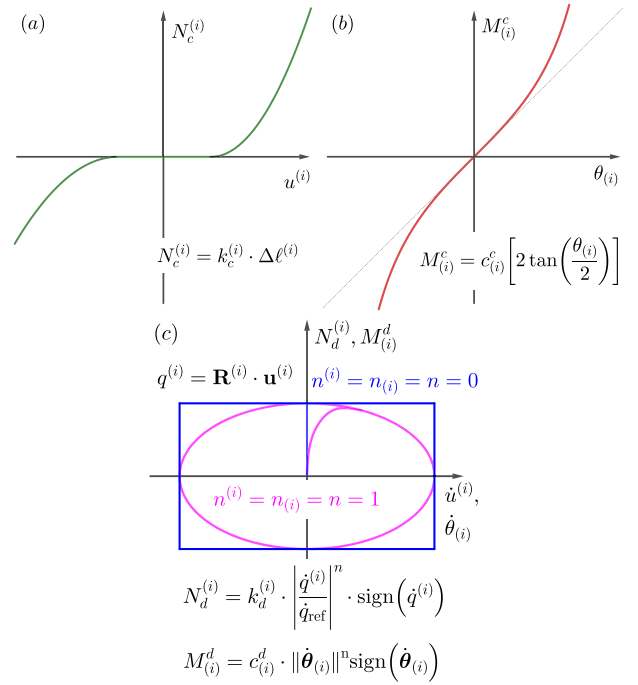

Fig. 5. The constitutive relation of (a) axial spring (b) rotational spring and (c) axial and rotational dashpot of the lumped chain model.

$$N_c^i = k_c^i \cdot [\lambda^i - 1/(\lambda^i)^2], \quad \lambda^i = \ell^i(t)/\ell^i(t=0); \quad N_c^i = k_c^i \cdot q^i \tag{13}$$

where the stretch $\lambda^i = 1 + \epsilon^i$ in which $\epsilon^i \equiv \Delta \ell^i / \ell^i(t=0)$ is the small strain, $\dot{q}_{\mathrm{ref}}$ is a reference velocity equal to 1 m/s. Both effective axial stiffness parameter k_d^i and dissipation parameters k_c^i and n can be non-linearly dependent on the basic unknowns, see Fig. 5.

3.1.2. Contact model

An axial contact model with gap opening and closing is used to constrain the total axial length change $\Delta \ell^i$ of each element (Fig. 6). The initial stress-free maximum length of a bar-element i is ℓ_0^i. Applying the axial forces, the length changes to $\ell^i = \ell_0^i + \Delta \ell^i$, which can be positive or negative. The contact gap variable d^i (Fig. 6) is defined as follows:

$$0 \approx d_{min} \leq d^i \leq d_{max} = \Delta \ell^i + d^i \tag{14}$$

where the axial elongation or compression of an arbitrary ith bar-element is given simply by its length-change $\Delta \ell^i$.

The internal elastic force N_c^i is determined in the following manner depending on d^i together with the gap opening–closing conditions (Fig. 6):

(i) Gap opening ($\dot{\ell}^i \geq 0$) over the maximum opening $d^i \geq d_{max}$ and resisting restoring elastic stretching force, $N_c^i > 0$

(ii) Gap opening ($\dot{\ell}^i \geq 0$) or closing ($\dot{\ell}^i \leq 0$) with $d_{min} \approx 0 < d^i < d_{max}$ without elastic resistance (neutral), $N_c^i = 0$

(iii) Gap closing ($\dot{\ell}^i < 0$) beyond the maximum closing d_{min} (small inter-penetrability) and resisting elastic compression, $N_c^i < 0$

Note that the dissipative axial forces are not set to zero during the gap opening or closing because friction is still present. Note as well that each bar-element's contact gap d^i is different. Finally, note that the sign of axial length change $\Delta \ell^i$ is the same as the sign of the change contact gap, so $\operatorname{sign}(\dot{d}^i) = \operatorname{sign}(\dot{\ell}^i)$ and therefore, the opening ($\dot{\ell}^i \geq 0$) or closing ($\dot{\ell}^i < 0$) of the contact gap can be detected by equivalently the sign of $\dot{d}^i$ or $\dot{\ell}^i$.

The contact behavior is implemented through an effective constitutive response. The axial deformation $\Delta \ell^i$ can open or close the gap $d^i \in [d_{min}, d_{max}] \equiv \mathrm{G}$. Gap opening occurs when $\dot{d}^i \geq 0$ and, reciprocally, closing occurs for $\dot{d}^i < 0$. Opening or closing the gap within $d_{min} \leq d^i \leq d_{max}$ occurs without elastic resistance. In this case, an effective elasticity
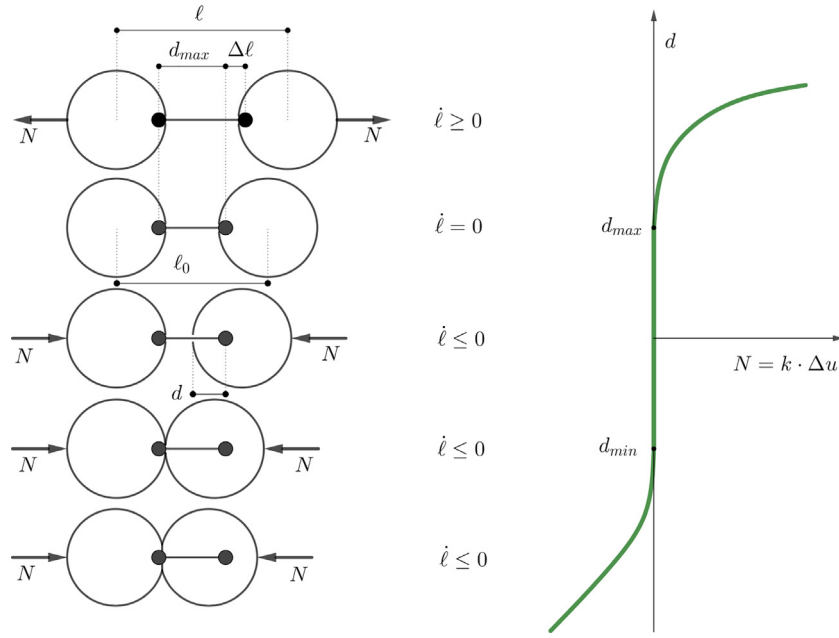
Fig. 6. Physical meaning of the conservative axial constitutive law: two beads of the chain when chain is extended and when the beads collide (gap-contact model), note that the index i has been dropped for clarity.
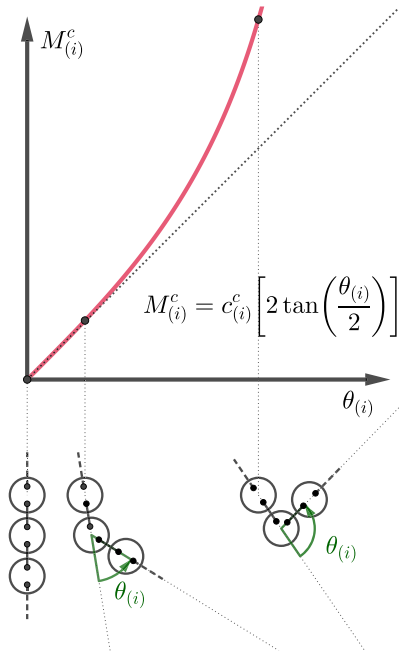

Fig. 7. Physical meaning of the rotational conservative constitutive law: three beads at different angles.

coefficient K_s^i is set equal to zero. Closing, a small inter-penetrability is allowed, the gap beyond $|d^i| \geq d_{min}$ occurs elastically with an elasticity coefficient K_{sc}^i. After stretching, opening the gap beyond $d^i \geq d_{max}$, the material elastic response is coded into the effective elasticity coefficient K_{so}^i.

Then the elasticity coefficient in the constitutive relation for the axial (elastic) internal force N_c^i is given as:

$$N_c^i = k_c^i \cdot \Delta\ell^i = k_c^i \cdot q^i$$

$$k_c^i = I_G(d^i) \cdot K_s^i = I_G(d^i) \cdot \begin{cases} K_{so}^i, & \text{if } \dot{d}^i \geq 0 \\ K_{sc}^i, & \text{if } \dot{d}^i < 0 \end{cases} \quad ; \quad I_G(d^i) = \begin{cases} 1, & \text{if } d^i \notin G \\ 0, & \text{if } d^i \in G \end{cases}$$

where $I_G(d^i)$ is the indicator function. To obtain a finite (bounded) energy potential of contact at threshold values d_{min} and d_{max} (potential walls), a smooth approximation of the indicator function is used:

$$I_G(d^i, \dot{d}^i) = \begin{cases} \frac{1}{2}\left(1 + \tanh[c_1^i(\Delta\ell^i - d_{max})/d_{max}]\right), & \text{if } \dot{d}^i \geq 0 : \text{ gap opening} \\ \frac{1}{2}\left(1 - \tanh[c_1^i(\Delta\ell^i + d_{min})/d_{max}]\right), & \text{if } \dot{d}^i < 0 : \text{ gap closing}, \end{cases}$$

(16)

where c_1^i is a constant.

3.1.3. Bending internal nodal force

The internal nodal forces $\boldsymbol{f}_i(M)$ due to bending moment M_i at joint i are formed as column vectors of size (6×1) through the resistance of relative rotation θ_i:

$$\delta W_{\text{int}}(M) = \sum_i M_i \delta\theta_i = \sum_i \delta\tilde{\mathbf{u}}_i^T \left(M_i \cdot [\nabla_{\tilde{\boldsymbol{x}}_i}\theta_i]^T \right) \equiv \sum_i \boldsymbol{f}_i(M) \cdot \delta\mathbf{u}_i \quad (17)$$

$$\boldsymbol{f}_i(M) = [M_i^c + M_i^d] \cdot [\nabla_{\tilde{\boldsymbol{x}}_i}\theta_i]^T, \quad \text{for } i = 2 : N - 1 \quad (18)$$

Note that $\nabla_{\tilde{\boldsymbol{x}}_i}\theta_i$ is taken with respect to the coordinates $\tilde{\boldsymbol{x}}_i = [\boldsymbol{x}_{i-1}, \boldsymbol{x}_i, \boldsymbol{x}_{i+1}]^T$ of the nodes $i - 1$, i and $i + 1$ since $\theta_i = \theta_i(\boldsymbol{x}_{i-1}, \boldsymbol{x}_i, \boldsymbol{x}_{i+1})$ is function of the independent coordinates. The conservative and dissipative bending moments are determined by a relevant constitutive relation $M_i = f(\kappa_i(\tilde{\mathbf{u}}_i), c_i)$. The constitutive relation for the dissipative (viscous/friction) M_i^d and the conservative M_i^c moment at node i is of the form :

$$M_i^d = c_i^d \cdot \|\dot{\theta}_i\|^n \text{sign}(\dot{\theta}_i) \quad (19)$$

$$M_i^c = c_i^c \left(2 \tan(\theta_i/2)\right) \quad (20)$$

For illustration purposes, the nodal generalized viscous/friction forces are shown in Fig. 5. The rate of relative rotation at node number i can be shown to be

$$\dot{\theta}_i = [\nabla_{\tilde{\boldsymbol{x}}_i}\theta_i]\dot{\tilde{\mathbf{u}}}, \quad (21)$$

where

$$\dot{\tilde{\mathbf{u}}} = (\dot{x}_{i-1}, \dot{y}_{i-1}, \dot{x}_i, \dot{y}_i, \dot{x}_{i+1}, \dot{y}_{i+1}) \quad (22)$$
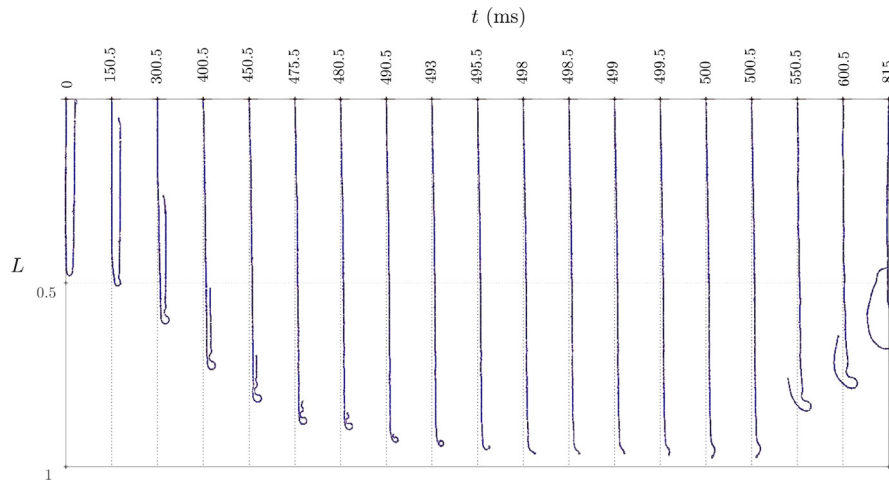
Fig. 8. Unfolding of the folded chain for the case of test T2.

Table 2
The parameters of the mechanical model.

Parameters							
Geometric		Inertial		Conservative		Dissipative	
NE	100	M (g)	31	k_c^i (N/m)	$9.21 \cdot 10^5$	k_d^i (N)	$10.5 \cdot 10^6$
ℓ^i (mm)	15.1	m (g/m)	21	c_i^c (N/m rad)	$0.789 \cdot 10^{-3}$	c_i^d (N m s/rad)	$0.79 \cdot 10^{-4}$
L (mm)	1512			c_1^i	10	n	1

Fig. 7 demonstrates the physical interpretation of the rotational conservative law. As the rotation $\theta_{(i)}$ increases the bending resistance of the chain increases. More specifically, after a certain angle $\theta_{(i)}$, the chain "locks" and the resistance increases with much higher rate than for smaller angles.

4. Results and discussions

The parameters of the mechanical model are presented in Table 2. The tensile axial resistance has been experimentally verified, while the rest of the parameters were chosen by using engineering judgement. The patterns of the folded free-falling chain are demonstrated in Figs. 8 and 9 for the tests T2, T4 and T5. The horizontal distance between vertical dotted lines in Figs. 8 and 9 is equal to the opening d_o for each case, while in Fig. 9 the dash-dotted line is located midway between the dotted lines, namely at horizontal distance $d_o/2$ from both of them.

Furthermore, the post-processing of the digital images and the production of the data, namely location (coordinates as a function of time) of the chain's tip, has been extracted according to the work of Trujillo-Pino et al. [34]. The normalized vertical displacement y/L along with the normalized vertical velocity $\dot{y}/gt$ (g is the gravitational acceleration) and the normalized vertical acceleration $\ddot{y}/g$ of the chain's tip of three tests, namely T2, T4 and T5, are shown in Figs. 10, 11 and 12 respectively. More specifically, the subplots (a) of Figs. 10, 11 and 12, show the normalized vertical displacement of the folded chain's tip compared to the vertical normalized displacement of the free fall are plotted against normalized time $t/\sqrt{2L/g}$. The vertical displacement of the free fall is given as:

$$y_f = -\frac{1}{2}gt^2 \qquad (23)$$

In the subplots (b) of Figs. 10, 11 and 12 the normalized displacement is plotted against time t. In the subplots (c) and (d) of Figs. 10, 11 and 12, the normalized vertical velocity $\dot{y}/L$ and the normalized vertical acceleration $\ddot{y}/g$, respectively, are plotted against time t. It is worth mentioning that the velocity and acceleration data have been smoothed using the Savitzky–Galoy filter [35,36]. Additionally, a comparison between the three tests (T2, T3 and T5) is implemented in Fig. 13 for all the aforementioned kinematic variables.

The results of the falling patterns can be grouped into three phases: the unfolding phase, the whipping phase, and the rebounding phase, see Fig. 14 for the case of test T2. The unfolding phase includes the falling of the tip, the whipping phase at which the direction of the vertical motion of the tip changes sign, and the rebounding phase at which the tip has already changed the direction of motion and moves upwards.

During the unfolding phase, contrary to the educated intuition, the tip of the folded chain falls faster than the free-fall (see subplot (a) of Figs. 10, 11, 12 and 13) due to the conservation of linear momentum and the reduction of the amount of moving mass, [9]. Moreover, in all cases (T2, T4, and T5), the vertical velocity of the tip is larger than gt, while the vertical acceleration is larger than g for most of the falling time, see subplot (c) and (d) Figs. 10, 11, 12 and 13. Additionally, during the falling phase, the behavior of the chains is affected by the initial opening d_o, see Fig. 1 and falling time t_f is different for different set-ups, see Fig. 13(b). More specifically, in the case of opening $d_o = 0.045$ m (i.e. test T2) the falling part is almost vertical (see Fig. 8), while in the case of $d_o = 0.087$ m (test T4) and $d_o = 0.128$ m (test T5), the falling part is inclined, which results in a wavy shape (see for instance the falling part of test T4 at $t = 200$ ms, Fig. 9(a)). The non-moving part of the folded chain in all cases as the time goes by, tends to an inclined straight line shape towards the moving part, see Fig. 8 from $t = 0$ ms to $t = 498$ ms, Fig. 9(a) from $t = 0$ ms to $t = 449$ ms and Fig. 9(b) from $t = 0$ ms to $t = 434$ ms. Furthermore, the lower segment of the falling part of the chain buckles locally, which is a phenomenon clearly demonstrated in the case of test T2 but also in the cases of T4 and T5, see Figs. 8 and 9. Fig. 14(a) demonstrates a section of the falling part of the folded chain of test T2, which is caused by the fact that the upper part (point A) of the falling part moves faster (larger acceleration) than the lower one (point B). Consequently, the upper part introduces a larger force ($P + \Delta P$) compared to the lower part (force P) in the falling part of the chain. In other words, the falling part AB of the chain, shown in Fig. 14(a), is subjected to non-uniform compression. The falling part of the chain for the case of test T5 enters faster than the other two tests (T2, T4) the whipping phase, a direct consequence of the larger d_o, which results in a smaller h distance, see Figs. 1 and 13.
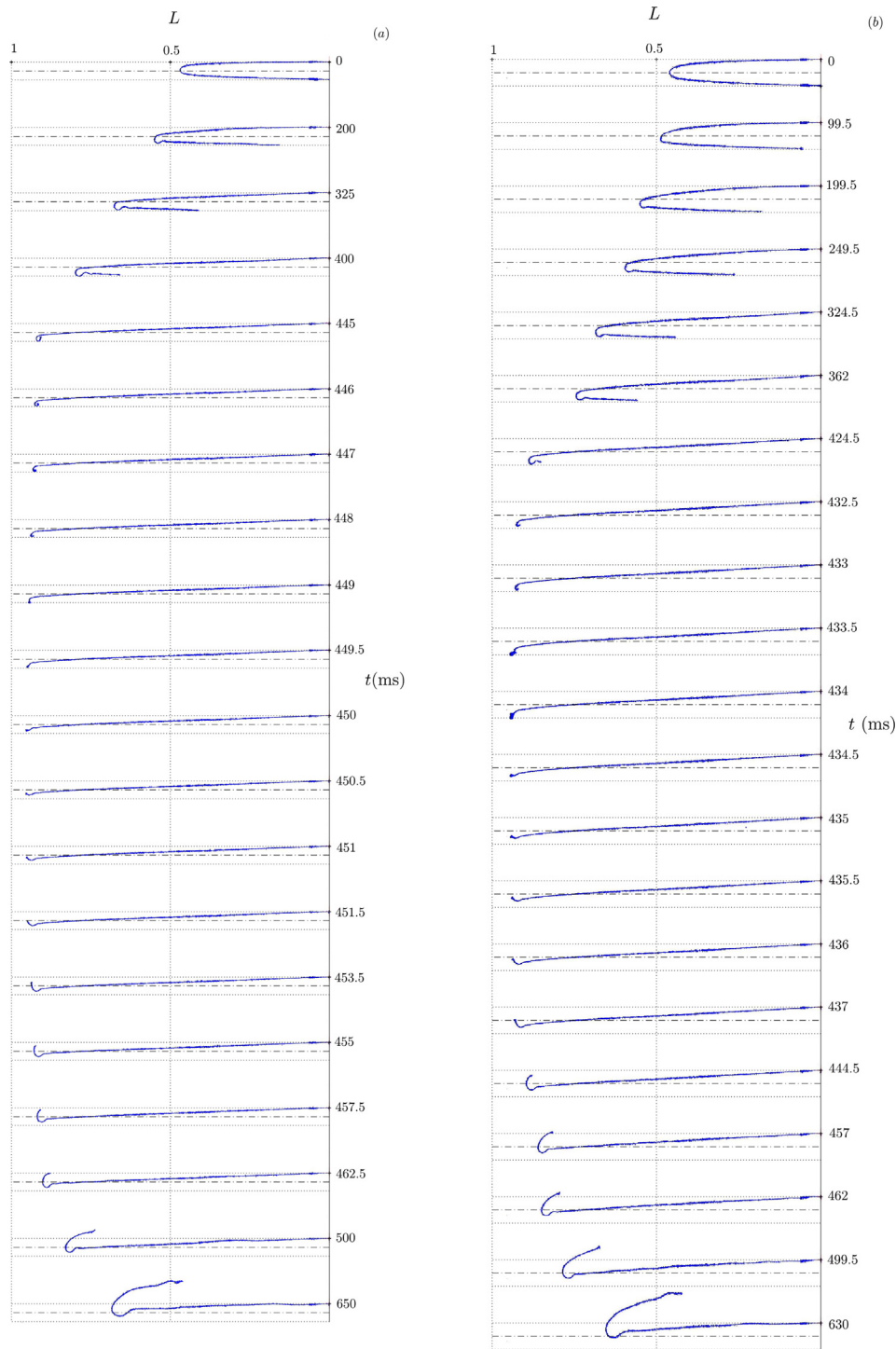
**Fig. 9.** Unfolding of the folded chain for the case of (a) test T4 and (b) test T5.

Various interesting phenomena occur during the whipping phase, see Fig. 14(b). First of all, the sign of the vertical displacement of the tip changes, which results in a jump in the velocity graph (see subplot (c) of Figs. 10, 11, 12 and 13), and this results in very high values of acceleration as compared to g (see subplot (c) of Figs. 10, 11, 12 and 13). During this phase, the chain behaves like a whip by changing the direction of vertical motion, see Figs. 8, 9 and 14(b). The whipping effect can be explained as follows: the moving mass of the folded falling chain tends to zero. Since the momentum is conserved, the velocity tends to infinity, [15,16]. Consequently the chain does not

become straight but instead changes direction in a similar manner, if not identical, to the whip.

The consequence of the whip effect is the generation of transverse wave propagation directed upwards during the rebounding phase [15], which is demonstrated in Fig. 14(d). The upward transverse shock wave velocity can be calculated by using the digital sequence of images shown in Fig. 14(b). The velocity of the transverse waves c, can be expressed in terms of the tension T in the chain as follows:

$$c = \sqrt{\frac{T}{\mu}} \Leftrightarrow T = \mu c^2 \tag{24}$$
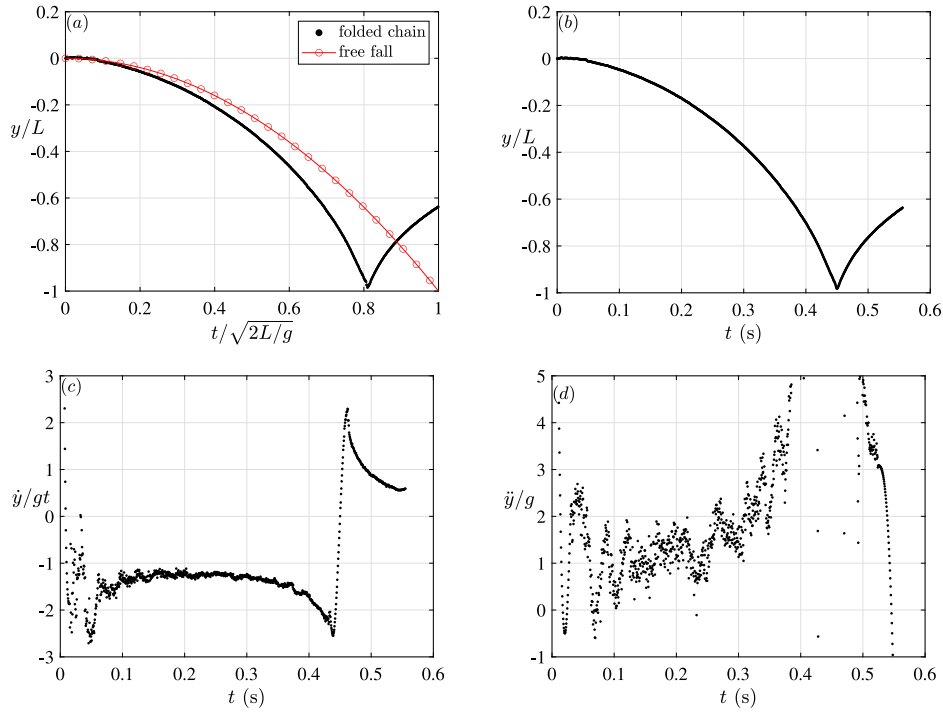
Fig. 10. For the case of test T2: (a) normalized vertical displacement of folded chain compared to free fall, (b) normalized vertical displacement, (c) normalized vertical velocity and (d) vertical acceleration.
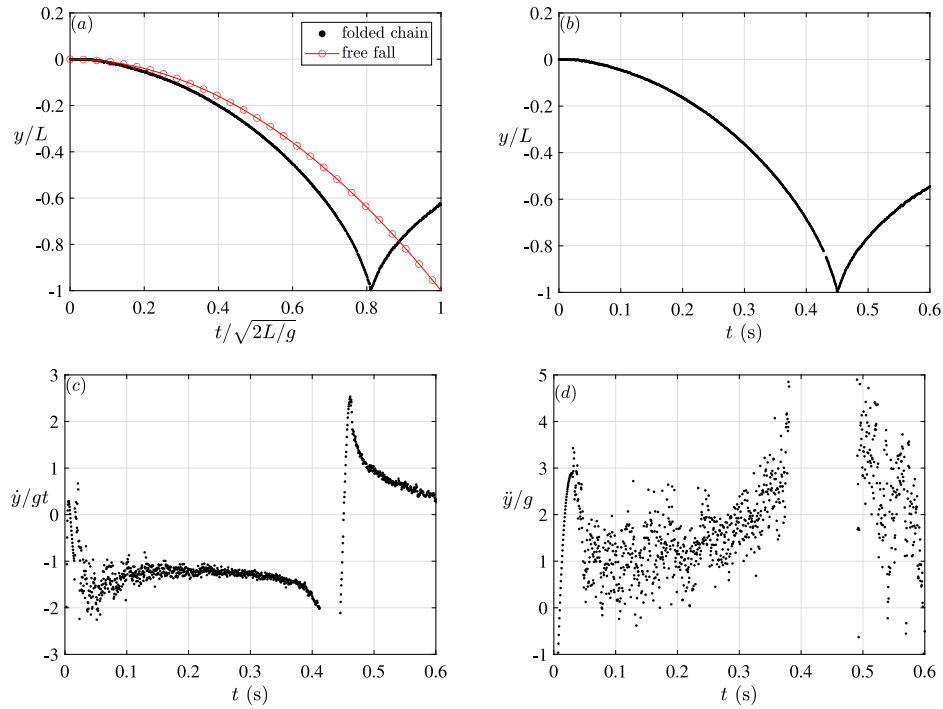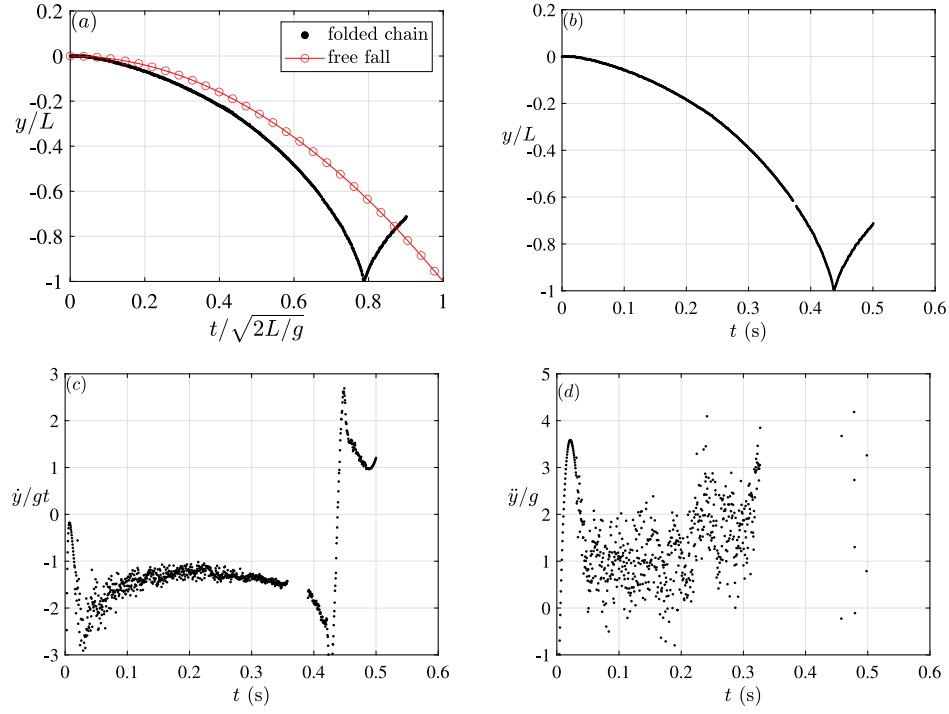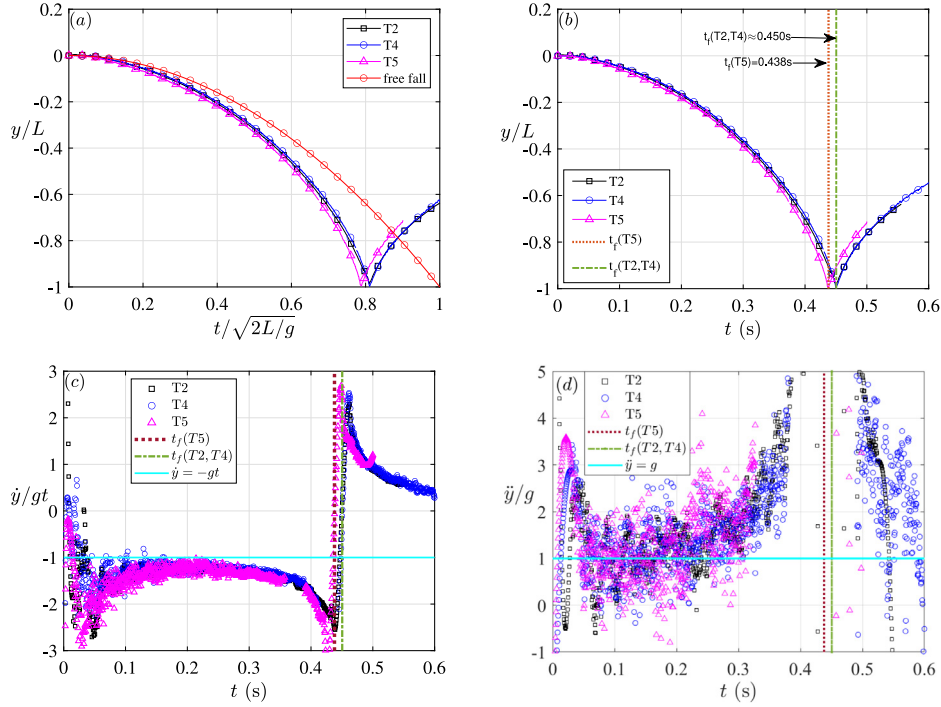

Fig. 11. For the case of test T4: (a) normalized vertical displacement of folded chain compared to free fall, (b) normalized vertical displacement, (c) normalized vertical velocity and (d) vertical acceleration.

By using the data from Fig. 14(b), the wave velocity is estimated to be $c = 15$ m/s. Since the total mass of the chain is equal to $M = \mu L \approx 0.031$ kg (see Table 2), the tension from Eq. (24) can be calculated $T = 4.7$ N. Therefore the ratio of tension T to the self-weight of the chain Mg is $T/Mg \approx 17 \div 15$ times [9]. The rebound effect, which is demonstrated in

Fig. 14(c), causes the chain to move upwards after the whipping phase due to the stored strain energy in the system. During the rebounding phase of tests T2, T3, and T5, the tip of the chain opens more when the opening d_o is larger, with the extreme case being the pendulum behavior as the opening d_o approaches the length of the chain L.

Fig. 12. For the case of test T5: (a) normalized vertical displacement of folded chain compared to free fall, (b) normalized vertical displacement, (c) normalized vertical velocity and (d) vertical acceleration.

Fig. 13. Comparison for the case of tests T2, T4, T5: (a) vertical displacement of folded chain compared to free fall, (b) vertical displacement, (c) vertical velocity and (d) vertical acceleration.

The results of the numerical simulation are demonstrated in Fig. 15. The numerical model qualitatively captures the behavior of experimental tests. More specifically, the model is able to capture the local buckling (Fig. 15(a)) of the falling part of the chain in the unfolding phase. In addition the model effectively reproduces the whipping effect (Fig. 15(b)) during the whipping phase and the rebound effect (Fig. 15(c)) during the rebounding phase. Furthermore, the model captures the transverse wave propagation in the last time instants of
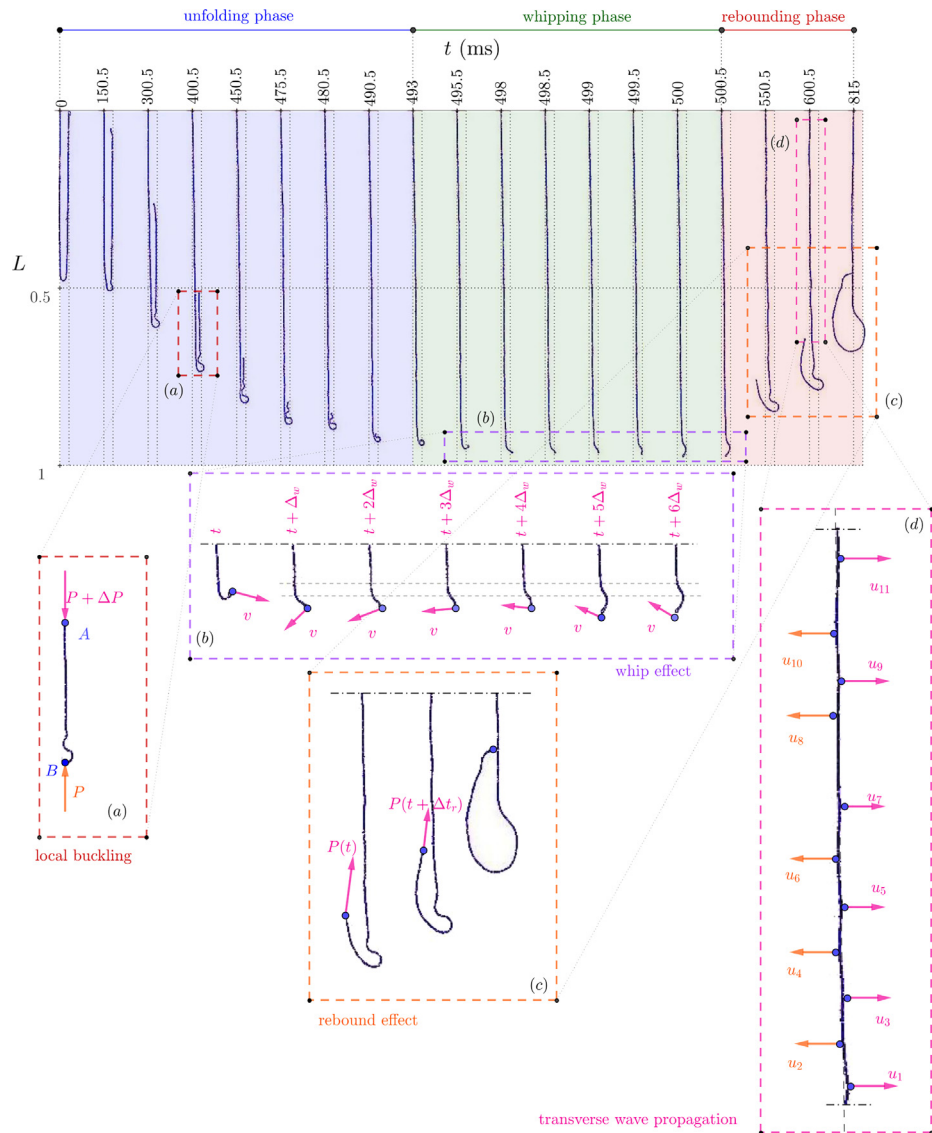
Fig. 14. For the case of test T2: (a) local buckling, (b) whip effect, (c) rebound effect and (d) transverse wave propagation phenomena observed at different phases: unfolding, whip, rebound.
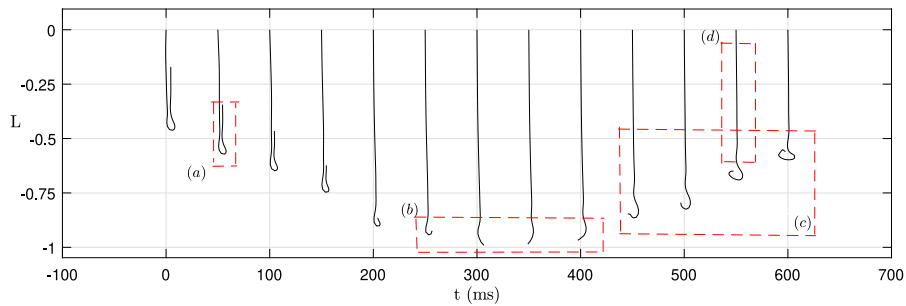

Fig. 15. Unfolding of the folded chain using the numerical model.

Fig. 15(d). Finally, the comparison of the model's falling time and the free fall are presented in Fig. 16.

It is also worth mentioning the uncertainties introduced by the current study's experimental and post-processing phases. More precisely, the uncertainties of the experiment can be organized into three categories. In the first category, the uncertainties are related to the setup of the experimental session. In the second category, the uncertainties are associated with the recording device, while in the third category,

the uncertainties are related to the post-processing procedure of the recorded data. In the first category, the uncertainties are linked to the following main issues: (i) zero initial velocity introduced during the release phase of the tip by burning the string *AP* (Fig. 1), (ii) planar motion of the chain perpendicular to the camera (iii) rigidity and dissipation of the fixation point (point *O* in Fig. 1) and (iv) lighting of the chain. In the second category, the recording device's limitations
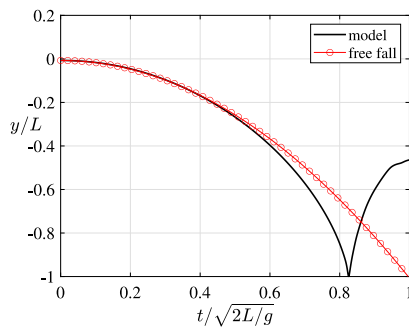
Fig. 16. Comparison of vertical displacement reproduced by the mechanical model of folded chain compared to free fall.

introduce uncertainty in the recording process of the frames. Since the speed of the chain increases during the falling stage and decreases during the rising stage, the high-speed frame rate should be proceeded to avoid the loss of details. However, using a higher frame rate need more memory for the data. Compromising the frame speed and duration creates uncertainties during the chain falling stage due to the high speed of the chain during the whipping phase. Finally, the uncertainties regarding the post-processing phase of the analysis are associated with identifying the tip's position algorithm and, more specifically, the pixels transformation to coordinates (x_i, y_i). During the post-processing, the accuracy of the edge detecting highly depends on the focusing and light intensity. The accurate focusing and homogeneous light intensity can reduce the blurry of the chain edge. In this study, the blurry of the chain edge is around 1–2 pixels, corresponding to 1.58–3.16 mm uncertainties in the chain's tip location.

5. Conclusions

In the current study the detailed sequences of the dynamic geometry of the unfolding of the falling folded chain have been studied. Experimental implementations of high-speed imaging (up to 10 000 fps) produced excellent resolution digital image sequences of different phases of falling U-chain dynamics. Three different setups have been used to investigate the phenomenon by varying the initial opening between the tips of the chain d_o (Fig. 1). The post-processing of the captured images provided the tip's vertical displacement time series, which for all cases was faster than the free-falling displacement. The quantitative data of displacement, velocity, and acceleration of the chain's tip in the various experimental setups have been reported, which can be used to validate numerical models. More importantly, the distinguishable different dynamical phases of the falling folded chain have been identified and categorized into three phases of unfolding, whipping and rebounding. The high-speed imaging uncovered a variety of phenomena such as: local buckling, whip effect, rebound effect and transverse wave propagation. In addition, a consistent discrete Henky-type mechanical model has been presented that was able to capture all the observed physical phenomena from the nonlinear dynamic behavior of the chain, clearly demonstrated by the experimental sessions. More specifically, the model is capable of describing the complex nonlinear interaction forces between the beads of the chain by including nonlinear elastic, dissipative and bilateral gap-contact features. The subject of the next part of our study deals with the extension of the model into the 3rd dimension to capture the complex dynamic behavior of cables.

CRediT authorship contribution statement

Athanasios A. Markou: Conceptualization, Methodology, Writing – original draft, Software, Writing – review & editing, Validation, Investigation, Data curation, Visualization, Supervision, Project administration, Formal analysis. **Djebar Baroudi:** Conceptualization, Methodology, Software, Writing – original draft, Software, Writing – review &

editing, Investigation, Project administration, Formal analysis. **Qiang Cheng:** Data Curation, Resources, Validation, Investigation, Formal analysis. **Hadi Bordbar:** Writing – original draft, Supervision, Visualization.

Declaration of competing interest

The authors declare that they have no known competing financial interests or personal relationships that could have appeared to influence the work reported in this paper.

Data availability

Data will be made available on request.

Appendix A. Supplementary data

Supplementary material related to this article can be found online at https://doi.org/10.1016/j.ijnonlinmec.2022.104257.

References

[1] L. Meirovitch, General motion of a variable-mass flexible rocket with internal flow, J. Spacecr. Rockets 7 (2) (1970) 186–195.
[2] F. Bouaziz-Kellil, Motion of the infinitesimal variable mass in the generalized circular restricted three-body problem under the effect of asteroids belt, Adv. Astron. (2020).
[3] E. Canessa, Modeling of body mass index by Newton's second law, J. Theoret. Biol. 248 (4) (2007) 646–656.
[4] S. Siegel, More about variable mass systems, Amer. J. Phys. 40 (1) (1972) 183–185.
[5] L. Casetta, Equivalence theorem between position-dependent mass dynamics and classically conservative dynamics, Int. J. Non-Linear Mech. 100 (2018) 30–33.
[6] E. Canessa, Stock market and motion of a variable mass spring, Physica A 388 (11) (2009) 2168–2172.
[7] A.R. Plastino, Juan Muzzio, On the use and abuse of Newton's second law for variable mass problems, Celest. Mech. Dynam. Astron. 53 (1992) 227–232.
[8] H. Irschik, H.J Holl, Mechanics of variable-mass systems—Part 1: Balance of mass and linear momentum , Appl. Mech. Rev. 57 (2) (2004) 145–160.
[9] M.G. Calkin, R.H. March, The dynamics of a falling chain: I, Amer. J. Phys. 57 (2) (1989) 154–157.
[10] C.W. Wong, K. Yasui, Falling chains, Amer. J. Phys. 74 (6) (2006) 490–496.
[11] C.E. Mungan, Newtonian analysis of a folded chain drop, Phys. Teach. 56 (5) (2018) 298–301.
[12] A. Cayley, VIII. On a class of dynamical problems, Proc. R. Soc. Lond. 8 (1857) 506–511.
[13] D. Kagan, A. Kott, The greater-than-g acceleration of a bungee jumper, Phys. Teach. 34 (6) (1996) 368–373.
[14] M. Schagerl, A. Steindl, W. Steiner, H. Troger, On the paradox of the free falling folded chain, Acta Mech. 125 (1997) 155–168.
[15] J. Taft, The propagation of waves through a cracking whip, Acta Mech. (2003).
[16] A. Goriely, T. McMillen, Shape of a cracking whip, Phys. Rev. Lett. 88 (2002) 244301.
[17] W. Tomaszewski, P. Pieranski, Dynamics of ropes and chains: I. The fall of the folded chain, New J. Phys. 7 (2005) 45.
[18] P. Fritzkowski, H. Kamiński, Dynamics of a rope modeled as a discrete system with extensible members, Comput. Mech. 44 (2009) 473–480.
[19] W. Tomaszewski, P. Pieranski, J.-C. Geminard, The motion of a freely falling chain tip, Amer. J. Phys. 74 (9) (2006) 776–783.
[20] J.-C. Géminard, L. Vanel, The motion of a freely falling chain tip: Force measurements, Amer. J. Phys. 76 (6) (2008) 541–545.
[21] A. Heck, P. Uylings, E. Kedzierska, Understanding the physics of bungee jumping, Phys. Ed. 45 (1) (2009) 63–72.
[22] C.A. de Sousa, P.M. Gordo, P. Costa, Falling chains as variable-mass systems: theoretical model and experimental analysis, Eur. J. Phys. 33 (4) (2012) 1007–1020.
[23] H. Yokoyama, Reexamining the chain fountain, 2018.

[24] A.A. Domnyshev, V.A. Kalinichenko, P.M. Shkapov, On two experiments with falling chains, J. Phys. Conf. Ser. 1301 (2019) 012012.

[25] W. Guttner, C. Pesce, On Hamilton's principle for discrete systems of variable mass and the corresponding Lagrange's equations, J. Braz. Soc. Mech. Sci. Eng. 39 (2016) 1–8.

[26] H.-H. Lee, C.-F. Chen, I.-S. Hu, Solving the paradox of the folded falling chain by considering the link transition and link geometry, Acta Mech. 230 (2019).

[27] E. Virga, Chain paradoxes, Proc. R. Soc. A 471 (2014).

[28] Emilio Turco, Francesco dell'Isola, Anil Misra, A nonlinear Lagrangian particle model for grains assemblies including grain relative rotations, Int. J. Numer. Anal. Methods Geomech. 43 (5) (2019) 1051–1079.

[29] E. Turco, F. dell'isola, A. Cazzani, N. Rizzi, Hencky-type discrete model for pantographic structures: numerical comparison with second gradient continuum models, Z. Angew. Math. Phys. 67 (2016).

[30] Photron Fastcam SA-Z, 2016, https://photron.com/fastcam-sa-z-2/.

[31] MATLAB, version 7.10.0 (R2022a), The MathWorks Inc., Natick, Massachusetts, 2022.

[32] L.F. Shampine, M.W. Reichelt, The MATLAB ODE suite, SIAM J. Sci. Comput. 18 (1) (1997) 1–22.

[33] L.F. Shampine, M.W. Reichelt, J.A. Kierzenka, Solving index-i DAEs in MATLAB and simulink, SIAM Rev. 41 (3) (1999) 538–552.

[34] A. Trujillo-Pino, K. Krissian, M. Alemán-Flores, D. Santana-Cedrés, Accurate subpixel edge location based on partial area effect, Image Vis. Comput. 31 (1) (2013) 72–90.

[35] S.J. Orfanidis, Introduction to Signal Processing/Sophocles J. Orfanidis, in: Prentice Hall signal processing series, Prentice Hall, Englewood Cliffs, N.J., 1996.

[36] R.W. Schafer, What is a savitzky-golay filter? [lecture notes], IEEE Signal Process. Mag. 28 (4) (2011) 111–117.